metals

MDPI

Article

The Optimization of the Synthesis of Antibacterial Coatings on Ti6Al4V Coupons Obtained by Electron Beam Melting

Javier Molina [1,2,*], Ana Valero-Gómez [1], Patricia Bernabé-Quispe [3], María Ángeles Tormo-Mas [3] and Francisco Bosch [1]

[1] AIDIMME, Instituto Tecnológico Metalmecánico, Mueble, Madera, Embalaje y Afines, Parque Tecnológico, Avda. Leonardo Da Vinci, 38, 46980 Paterna, Spain; avalero@aidimme.es (A.V.-G.); fbosch@aidimme.es (F.B.)
[2] Departamento de Ingeniería Textil y Papelera, EPS de Alcoy, Universitat Politècnica de València, Plaza Ferrándiz y Carbonell s/n, 03801 Alcoy, Spain
[3] Grupo Infección Grave, Instituto de Investigación Sanitaria La Fe, Hospital Universitari i Politècnic La Fe, Avd. Fernando Abril Martorell 106, 46026 Valencia, Spain; patricia_bernabe@iislafe.es (P.B.-Q.); tormo_man@iislafe.es (M.Á.T.-M.)
* Correspondence: jamopue@upvnet.upv.es

Abstract: Prosthetic joint infection represents a problem that worsens the patient's quality of life and produces an economic impact on health systems. We report the anodization of Ti6Al4V coupons obtained by electron beam melting to produce a nanostructured surface. Anodization at 10 V produced TiO_2 nanopores with a diameter in the range of 15–20 nm. Thereafter, Ag nanoparticles (AgNPs) were deposited in three different ways to provide antibacterial functionality to the coatings: electrochemically, thermally, and chemically. The electrochemical method did not provide good coverage of AgNPs. At 0.1 V of synthesis potential, cubic, octahedral, and truncated octahedral Ag crystals were obtained. The thermal method provided a good distribution of AgNPs but it damaged the TiO_2 nanostructure. The chemical method showed the best distribution of AgNPs over the anodized surface and preserved the anodized nanostructure. For this reason, the chemical method was selected to perform further studies. Ag^+ release was monitored in simulated body fluid at 37 °C, reaching 1.86 mg Ag^+/L after 42 days. The antibacterial coating showed excellent antibacterial activity and inhibited biofilm formation for *Staphylococcus epidermidis RP62A and Staphylococcus aureus V329* strains (lethality > 99.9% for both bacteria and assays).

Keywords: antibacterial coating; silver ion; additive manufacturing; electron beam melting; Ti6Al4V

check for updates

Citation: Molina, J.; Valero-Gómez, A.; Bernabé-Quispe, P.; Tormo-Mas, M.Á.; Bosch, F. The Optimization of the Synthesis of Antibacterial Coatings on Ti6Al4V Coupons Obtained by Electron Beam Melting. *Metals* **2024**, *14*, 855. https://doi.org/10.3390/met14080855

Academic Editor: Andrea Di Schino

Received: 30 June 2024
Revised: 20 July 2024
Accepted: 23 July 2024
Published: 25 July 2024

Copyright: © 2024 by the authors. Licensee MDPI, Basel, Switzerland. This article is an open access article distributed under the terms and conditions of the Creative Commons Attribution (CC BY) license (https://creativecommons.org/licenses/by/4.0/).

1. Introduction

Additive manufacturing has emerged as a groundbreaking technique in the field of materials science due to advantages such as mass customization, waste minimization, the freedom of design that allows us to obtain complex nanostructures, fast production, etc. [1]. These properties have opened the application of additive manufacturing to polymers and composites [2], metals and alloys [3], ceramics [4], cement/concrete [5], wood [6], etc.

The Ti6Al4V alloy has been widely used in additive manufacturing for the production of items related to different fields such as in the aerospace, marine, automobile, energy, and chemical and biomedical industries [7]. Properties such as low density, high strength, high corrosion resistance, and biocompatibility make the Ti6Al4V alloy an optimal material for implants [7]. For Ti6Al4V, the main techniques used in advanced manufacturing are direct energy deposition (DED) [8], selective lase melting (SLM) [9], and electron beam melting (EBM) [10]. The use of additive manufacturing techniques to produce Ti6Al4V biomaterials and its surface modification has been widely reported in the literature [9,11–15]. Additive manufacturing techniques allow for the production of porous structures that mimic the mechanical behavior of bone, and these pores provide a supporting material where bone can grow, thus favoring osseointegration [11].

Implant-related infection and the detachment of implants from the bone due to poor osteointegration are two problems than can arise during implantation [16]. Bacterial proliferation affects numerous daily applications/products such as food [17], medical implants [18,19], surgical interventions [20], manufacturing and marine industries [21], and even spatial exploration [22]. Surfaces are particularly prone to bacterial colonization and biofilm formation [23,24]. Orthopedic implants are of vital importance for restoring functionality to patients that suffer from musculoskeletal diseases or traumatic injuries, and their implantation is constantly increasing due to an increased life expectancy [25]. However, the surgical implantation of orthopedic implants generates a risk of infection, with subsequent complications for patients and healthcare systems [26]. As a result, Orthopedic-Device-Related Infections (ODRIs) have been increasing in recent years. The estimated economic impact by 2030 was projected to be USD 1850 million [27]. ODRIs cause a deterioration in the well-being of the patients, as well as having an economic impact on healthcare systems. ODRIs normally require an antibiotic treatment that can last between 6 and 12 weeks [28], which can lead to implant extraction if the antibiotic treatment is not satisfactory [29]. Bacteria resistant to antibiotic treatment are increasingly being observed, which makes it necessary to research alternative ways to prevent and treat infections [30]. Also, biofilm formation is crucial in the development of these infections; bacteria stick on the surface of the material, developing a biofilm that allows them to evade the immune system and be up to 1000 times more resistant to antibiotic treatment [31]. *Staphylococcus* spp. (mainly *Staphylococcus aureus*) and coagulase-negative staphylococci (mainly *Staphylococcus epidermidis*) are the predominant causative organisms in ODRIs. These bacteria contribute to more than 50% of hip and knee prosthesis infections [32].

Several antibacterial agents can be included in coatings to produce functional antibacterial surfaces: peptides, organic and non-organic compounds, metal and non-metal compounds, classical antibiotics, etc. [33]. Inorganic agents such as Ag, Zn, or Cu (in the form of nanoparticles or as salts) provide an alternative to antibiotics in fighting bacterial infections [34]. It has been stated that the antibacterial capacity of these metals is correlated with the affinity for sulfur [34]. For instance, Ag^+, which is the antibacterial agent used in this paper, presents several modes of action against bacteria, which accounts for the lower resistance of bacteria to Ag^+ if compared to antibiotics [18]:

- The affinity of Ag^+ for thiol groups causes the death of microorganisms (since thiol groups comprise different proteins that play a key role in bacterial cells).
- Ag^+ can join and alter crucial enzymes for respiration and metabolism.
- Ag^+ can interfere in DNA division and replication processes.

As previously mentioned, osteointegration is crucial for prosthetic devices and is not always adequate with the bare Ti6Al4V alloy. Nanostructured surfaces are a way to improve osteointegration [16]. The modification of implant surfaces by zeolites [35], TiO_2 nanotubes and nanopores [36–38], hydroxyapatite [39,40], mesoporous silica [41], and other nanostructured biomaterials [42] has been reported to increase osteointegration.

The purpose of this work is to produce coatings on Ti6Al4V coupons obtained by EBM with antibacterial functionality. Ti6Al4V coupons are later anodized to produce a nanostructured surface containing nanopores around 15–20 nm in diameter. The function of the nanopores is to improve osteointegration, as has been reported in the literature [36–38]. AgNPs have been synthesized by three methods (electrochemical, thermal, and chemical) to provide a coating with antibacterial functionality. It was proven that the chemical method presented a good coverage of the anodized surface and a proper distribution of AgNPs, which would contribute to better antibacterial coatings.

2. Materials and Methods

2.1. Reagents and Materials

Distilled water: Distilled water was obtained from an ELGA Veolia Water and Milli-Q water was obtained from a direct-Q 3UV water purification system (for ICP-MS).

Ti6Al4V powders: Ti-6Al-4V grade 23 powder was acquired from AP&C company (Boisbriand, Canada) with the following size distribution (% by mass): <25 µm (0.1%), 25–45 µm (2.4%), 45–106 µm (94.6%), 106–150 µm (2.9%). The elemental mass composition was the following: Al (6.33%), V (4.03%), Fe (0.22%), O (0.22%), C (0.01%), N (0.01%), H (0.002%), Y (<0.001%), other (<0.4%), Ti (remainder).

Anodizing: sodium fluoride (Sigma Aldrich, St. Louis, MO, USA, ACS reagent ≥ 99.0%) and ammonium sulfate (Sigma Aldrich, ACS reagent ≥ 99.0%).

AgNPs synthesis: silver nitrate (Sigma Aldrich, BioXtra ≥ 99.0%)), sodium borohydride (Sigma Aldrich, Reagent Plus ≥ 99.0%), and ammonia (Panreac Ammonium solution reagent grade, 25% *w*/*w*).

Ag^+ release study: sodium chloride (Honeywell Fluka, Morris Plains, NJ, USA, ACS reagent ≥ 99.0%), sodium bicarbonate (Honeywell Fluka, ACS reagent Ph Eu. Powder ≥ 99.0%), potassium chloride (Honeywell Fluka, puriss. p.a. reagent ISO 99.5–100.5%), dipotassium phosphate (Scharlau, Barcelona, Spain, ACS reagent anhydrous), magnesium chloride hexahydrate (Honeywell Fluka, ACS reagent ≥ 99.0%), hydrochloric acid (Panreac AppliChem 37% for trace metal analysis), calcium chloride dihydrate (Panreac, Barcelona, Spain, powder PA-ACS), sodium sulfate (Honeywell Fluka, ACS reagent anhydrous powder ≥ 99.0%), tris(hydroxymethyl)aminomethane (Honeywell Fluka, puriss. p.a. ≥ 99.5%).

ICP-MS: nitric acid (69%, ultratrace, ppb-trace analysis grade) and silver (1000 mg/L standard solution) were acquired from Scharlau.

Antibacterial and biofilm formation test: glucose, Triptone Soya Agar (TSA), Triptone Soya Broth (TSB), and phosphate-buffered saline solution (7.4) were acquired from Scharlau (Barcelona, Spain).

2.2. General Plan of Experimental Work

Scheme 1 shows the general plan of experimental work that was carried out. After manufacturing the Ti6Al4V coupons using EBM, anodizing was optimized using three different voltages (10 V, 20 V, and 30 V). Thereafter, AgNPs were deposited on optimal anodized coupons by means of three deposition techniques (electrochemical, thermal, and chemical). The Ag^+ released in the simulated body fluid was studied for the optimal coating. Subsequently, antibacterial and antibiofilm characterization was performed for the optimal coating using *S. aureus* and *S. epidermidis* bacteria.

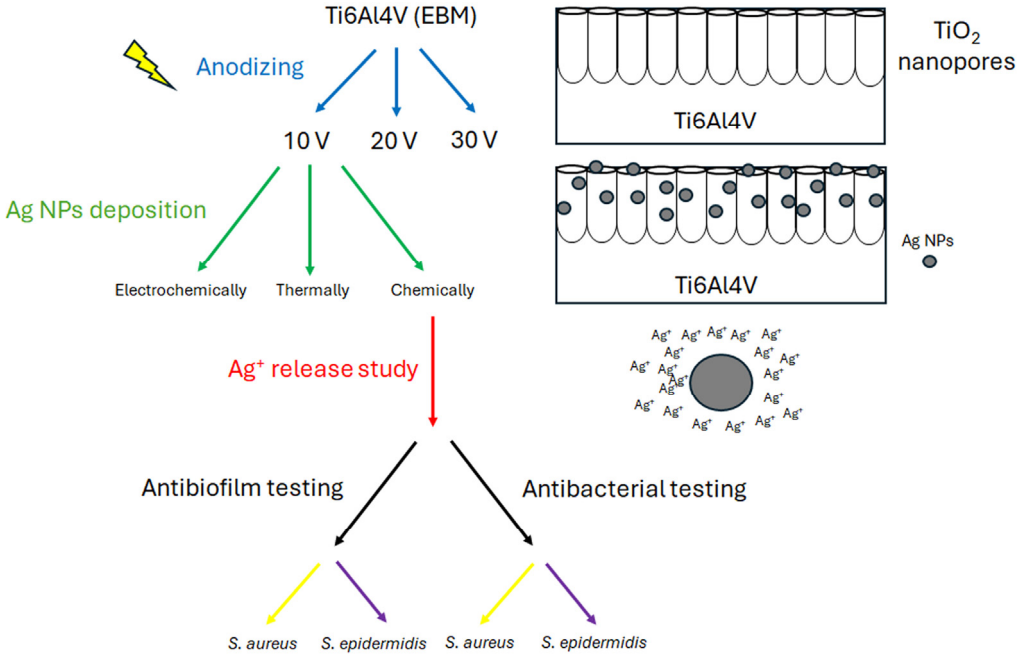

Scheme 1. General plan of experimental work carried out.

2.3. Fabrication of Additively Manufactured Ti6Al4V Coupons

Additively manufactured Ti6Al4V coupons were obtained with the electron beam melting technique (Arcam) using Ti6Al4V powder as the material source (high-vacuum and He atmosphere to inertize the atmosphere of the chamber). Before fusing each layer of metallic powder, it was pre-heated and sintered. The average fusion temperature obtained was around 1760 °C. The scan rate of the electron beam was 4600 mm/s with a spot of around 0.2 mm. The dimensions of Ti6Al4V coupons were 12 mm in diameter and 3.8 mm in thickness. A stick of Ti of 10 cm in length and 1.5 mm in diameter was also fabricated jointly with the Ti6Al4V piece to facilitate the electrical connection with the potentiostat/galvanostat. After carrying out anodization, this stick was cut.

2.4. Anodization of Ti6Al4V Coupons

A two-electrode configuration was used for anodizing. A thermostated electrochemical cell (500 mL) and a criothermostat from Julabo (600F Dyneo DD) were used to maintain the temperature during anodizing at 20 °C. A potentiostat/galvanostat (Metrohm, PGSTAT 302N) with the aid of a voltage multiplier (Metrohm) was used to achieve anodization potentials until 30 V. The working electrode was the additively manufactured Ti6Al4V piece, and a Pt mesh acted as the counter electrode, where a distance of 3 mm was maintained between both electrodes. Magnetic stirring was used during anodization to favor mass transfer. The solution employed for anodization consisted of 1 M $(NH_4)_2SO_4$ and 0.2% weight NH_4F. The anodization process was performed at 10 V, 20 V, and 30 V (for 4000 s) to determine the optimal anodization potential after HRFESEM observation and analysis of the microstructures obtained. Once the optimal anodization potential was determined (which was 10 V), different anodization times were performed at 10 V (500 s, 1000 s, 1500 s, 2000 s, 4000 s, and 8000 s). Anodized Ti6Al4V coupons were washed several times with distilled water after the anodization process and were thermally treated at 450 °C during 2 h in a muffle (Hobersal HD-150) to remove fluorides as much as possible and recrystallize amorphous TiO_2 into the anatase structure. The thermal treatment was applied at different moments depending on the synthesis route, as explained in Section 2.4.

2.5. AgNPs Synthesis

Three methods of the synthesis of AgNPs were applied:

- Electrochemical method of synthesis: A three-electrode configuration was employed; an anodized and thermally treated Ti6Al4V piece was used as the working electrode, Pt as the counter electrode, and a Ag/AgCl (3 M) as the reference electrode. The solution was $[Ag(NH_3)_2]^+$ (0.05 M $AgNO_3$ solution + NH_4OH until the yellow precipitate formed during NH_4OH addition was redissolved). Firstly, the potential was cycled using the potentiostat/galvanostat from 0.5 V to −0.5 V to determine at which potential Ag^+ reduction takes place. Thereafter, some potentials (0.1 V, 0.05 V, and 0 V) were selected to carry out a potentiostatic synthesis. In all cases, a −0.1 C electrical charge was achieved.
- Thermal method of synthesis: Anodized coupons were soaked for 1 h in $[Ag(NH_3)_2]^+$ (prepared as explained previously). Thereafter, a thermal treatment at 550 °C was applied for 2 h to produce the simultaneous recrystallization of TiO_2 and the reduction of Ag^+ to Ag^0.
- Chemical method of synthesis: This method of synthesis of AgNPs consisted of soaking the anodized coupons for 30 min in $[Ag(NH_3)_2]^+$. Thereafter, the samples were dipped in a 0.05 M $NaBH_4$ solution for 1 min to reduce Ag^+ to AgNPs. In another synthesis route, the samples were allowed to dry before the reduction stage. After that, the samples were washed with distilled water. Finally, the thermal treatment at 450 °C was applied.

2.6. High-Resolution Field-Emission-Scanning Electron Microscopy (HRFESEM)

A high-resolution field-emission-scanning electron microscope (HR-FESEM) (Zeiss GeminiSEM 500, Jena, Germany) was used to analyze the morphology of anodized samples as well as the distribution of AgNPs on the surface of the different samples using in-Lens and backscatter detectors. The samples were not coated with an additional conductive coating (Pt, Au, or C) due to the low acceleration voltage used (2 kV).

2.7. Ag^+ Release

The Ag^+ release study was performed in the samples where the best AgNP distribution was observed, which was the one obtained with the chemical method of the synthesis of AgNPs. The samples were dipped in 20 mL of Kokubo's simulated body fluid (SBF) [43] and incubated at 37 °C (the same temperature as in the human body) in a laboratory stove (Memmert). In total, 10 mL of the lixiviated SBF were extracted at different periods (1, 2, 4, 7, 14, 21, 28, 35, and 42 days) to carry out the ICP-MS analysis of the Ag concentration released. The extracted SBF was replaced with the same volume of fresh SBF.

The Ag^+ release in the SBF was determined by inductively coupled plasma/mass spectrometry (ICP-MS, Thermo Scientific iCAP RQ, Waltham, MA, USA). The sample injection system included a cooled Peltier at 3 °C and a cyclonic spray chamber to create a fine aerosol before introducing it into the system. Sampling was automated with a CETAC ASX-560 sampler. Calibration at seven different levels using calibration standards was performed. During the analysis, the masses were measured in scan mode using kinetic energy discrimination and the gas fluxes were 0.9 L/min of argon and 5.1 L/min of helium (collision gas).

2.8. Antibacterial Tests

2.8.1. Measurement of Antibacterial Activity

In the assessment of antibacterial activity, the strains *S. aureus* V329 and *S. epidermidis* RP62A were used. A slightly modified ISO 22196 [44] test was conducted to evaluate the antibacterial activity of the different surface-modified Ti6Al4V coupons. The differing strains were cultured at 37 °C on TSA overnight and then inoculated in 0.9% NaCl sterile solution to obtain bacterial solutions with a density of 5×10^5 colony-forming units (CFU)/mL. Sterilized additively manufactured Ti6Al4V coupons were located in sterile 24-well plates, and subsequently inoculated with 20 µL of the previously prepared bacterial suspension. A thin, sterile film covered the microbial inoculum, preventing surface evaporation and ensuring close contact with the antimicrobial surface. The coupons were incubated at 37 °C with a relative humidity of $\geq$90% for 24 h.

The film cover was removed after ending the incubation. Subsequently, the Ti6Al4V coupons (Ti6Al4V and anodized Ti6Al4V controls, and anodized Ti6Al4V + AgNPs coupons) were aseptically transferred to a tube containing 2 mL of TSB (tryptic soy broth). They underwent vortexing for 1 min at 2500 rpm, followed by sonication for 1 min at 50 kHz, and another vortexing step for 1 min at 2500 rpm. Parallel controls were performed at the beginning of the test and after the 24 h contact time. In total, 100 µL of the suspension and ten-fold serial dilutions were plated on TSA plates and incubated at 37 °C for 24 h to determine viable bacterial counts. Finally, the number of colonies was counted, and the reduction in microorganisms compared to their initial concentrations was calculated. Two coupons of each material were tested for each bacterium.

2.8.2. Biofilm Formation on Ti6Al4V Coupons

S. epidermidis RP62A and *S. aureus* V329 were used as high-biofilm-forming strains to evaluate biofilm formation. Suspensions of bacteria were prepared at a concentration of 1×10^6 CFU/mL in TSB and 0.25% w/v glucose to promote biofilm creation. Biofilm formation was tested on the surface of Ti6Al4V coupons (anodized Ti6Al4V + AgNPs and both controls Ti6Al4V and anodized Ti6Al4V), which were placed in 24-well polystyrene plates, with one disc per well. In total, 1 mL of bacterial suspension was added to each

well and was incubated for 48 h at 37 °C. Subsequently, the coupons were aseptically transferred into a tube, gently washed twice with sterile PBS to remove non-adherent cells, and then 1 mL of sterile TSB was added. The coupons were vortexed for 1 min at 2500 rpm, sonicated for 1 min at 50 kHz, and vortexed again for 1 min at 2500 rpm. In total, 100 µL of the suspension and ten-fold serial dilutions were plated on TSA plates and incubated to determine any viable bacteria adhered to the coupons. Finally, the number of colonies was counted, and the reduction in viable microorganisms attached to the coupons compared to the control was calculated. Six coupons of each material were tested for each bacterium, since biofilm testing normally presents more variability than antibacterial activity.

3. Results

3.1. Anodization of Ti6Al4V Coupons

Different anodization potentials were used to evaluate the best anodization potential for additively manufactured Ti6Al4V coupons. Potentials of 10 V, 20 V, and 30 V were tested, maintaining at this stage a synthesis time of 4000 s. Since a two-electrode configuration was used, the potential applied corresponds to the difference between the working electrode (Ti6Al4V) and the counter electrode (Pt mesh). The distance was maintained at 3 mm to reduce electrical resistance in the cell and facilitate the electron transfer. Figure 1 shows the chronoamperograms obtained during the anodization. In all the chronoamperograms, an initial large current density was observed, which is attributed to the initial oxide layer formation due to the applied potential and the oxidation of Ti to Ti^{4+}. The initial currents obtained after applying the anodization potential were 30 $mA{\cdot}cm^{-2}$, 48 $mA{\cdot}cm^{-2}$, and 73 $mA{\cdot}cm^{-2}$ for 10 V, 20 V, and 30 V, respectively. The initial current density increases with potential as does the thickness of the oxide layer formed. The current density rapidly decreases due to the formation of titanium dioxide via hydrolysis reaction [45] (Reaction (1)).

$$Ti^{4+} + 2H_2O \rightarrow TiO_2 + 4H^+ \quad (1)$$

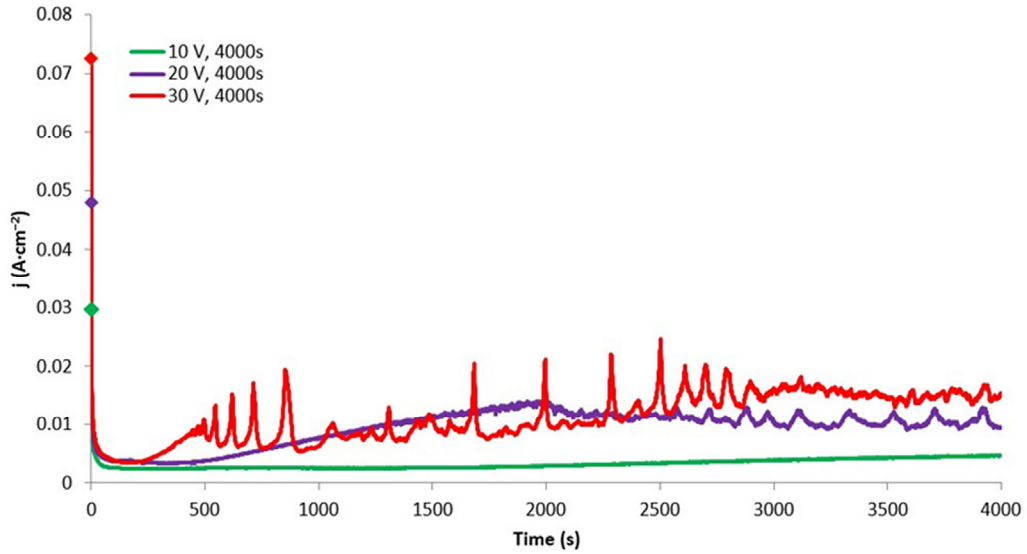

Figure 1. The chronoamperograms of the anodization of Ti6Al4V coupons obtained by additive manufacturing. Anodization potentials used: 10 V, 20 V, 30 V; anodization time: 4000 s; medium: 0.2% NH_4F and 1 M $(NH_4)_2SO_4$.

As can be seen from Reaction (1), the hydrolysis reaction tends to accumulate H^+ in the zones of TiO_2 formation. Fluorides which are contained in the anodizing solution migrate

to maintain electroneutrality. The TiO_2 dissolution and the formation of soluble H_2TiF_6 occurs when a critical F^- concentration is reached (Reaction (2)) [46].

$$Ti^{4+} + 2H^+ + 6F^- \rightarrow H_2TiF_6 \quad (2)$$

The dissolution of Ti^{4+} from the oxide produces vacancies in the oxide layer, and local negative charges are generated in the formed layer of oxides. These vacancies produce the oxidation of Ti to Ti^{4+} when migrating to the oxide/metal interface. An increase in the current density with time is observed in this phase due to the generation of nanoporosity on the oxide layer [46]. This phase was observed at all the applied potentials used in this work (Figure 1). If anodization proceeds the necessary time, the current density stabilizes due to the growth of the TiO_2 nanotubes [46].

In the second phase of synthesis, where current density tends to increase with time, at 10 V there was a steady increase in the anodization current with no sudden increase or decrease in the current density. In the case of 20 V anodization potential, there was a steady increase in current density until 2000 s, when it started to fluctuate. When 30 V of anodization potential was used, the current density increased rapidly, and after 500 s, large fluctuations appeared. These fluctuations are related to the cracking of the oxide layer (depassivation) and its regeneration (passivation), producing an alternate increase and decrease in the current density, respectively [46]. A higher fluoride concentration has been reported to produce more current density fluctuations due to the higher disolution rate achieved. The use of ethylene glycol in the electrolyte has been reported to reduce these fluctuations due to lower electrolyte conductivity [47]. In the present paper, when the potential increases, the current density oscillations appear earlier, and the amplitude of the oscillation also increased with the applied potential. Higher potentials increase the rate of TiO_2 dissolution, thus enhancing this effect. Considering the chronoamperograms obtained, the anodization at 10 V would be the most adequate, since the growth of the nanopores is continuous and does not present the breaking of the anodic layer. The anodization potential and the NH_4F concentration used (10 V and 0.2% NH_4F weight) is lower than the necessary amount required to anodize commercial Ti6Al4V rods (30 V and 0.4% NH_4F weight) [48].

HRFESEM was used to analyze the morphology of the samples obtained and select the best anodization potential based on the morphology observed. Figure 2 compares the micrographs at different magnifications (×5000, ×10,000, ×20,000) for the samples obtained at 10 V, 20 V, and 30 V. As can be seen at these magnifications, the anodization of the surface was general and not localized. At ×10,000 and ×20,000 magnification, the nanostructure of the anodized layer began to be observed and the finest nanostructure was obtained at 10 V.

The morphology of the nanostructures can be best evaluated when higher magnification was used (Figure 3), where ×50,000, ×100,000, and ×200,000 magnification was used. At 10 V, a homogeneous distribution of individual nanopores of 15–20 nm over the entire surface was obtained. Similar morphology has been reported in the literature [49]. At 20 V, the size of the nanopores increased to 25–40 nm and some of them joined together. At 30 V, the same happened, and some nanopores fused together and similar nanopore sizes were obtained. In general, an increase in the potential produces and increase in the nanopore/nanotube size [50]. Hence, the most adequate potential for anodizing was 10 V, where the individual nanopores were obtained without fusing together. The results observed by HRFESEM corroborate the ones obtained by the chronoamperograms, which showed a low fluctuation in the current density at 10 V when compared to 20 V and 30 V.

Once the anodization potential was optimized, the effect of anodization time on the morphology of the samples was evaluated. Different anodization times were tested (500 s, 1000 s, 1500 s, 2000 s, 4000 s, and 8000 s). The chronaomperograms obtained are shown in Figure 4. The features observed are the same as in Figure 1; an initial decrease in the current density in stage 1 (indicating the oxidation of Ti to Ti^{4+}) was observed for all synthesis times. In stage 2, there is an increase in the current density due to the formation of the nanopores; the growth of the nanopores depended on the synthesis time used. In stage 3,

there is a stabilization of the current density due to the TiO_2 nanotube growth; this stage was only observed for the anodization with the largest synthesis potential (8000 s), where the current density stabilized at around 6.7 $mA \cdot cm^{-2}$.

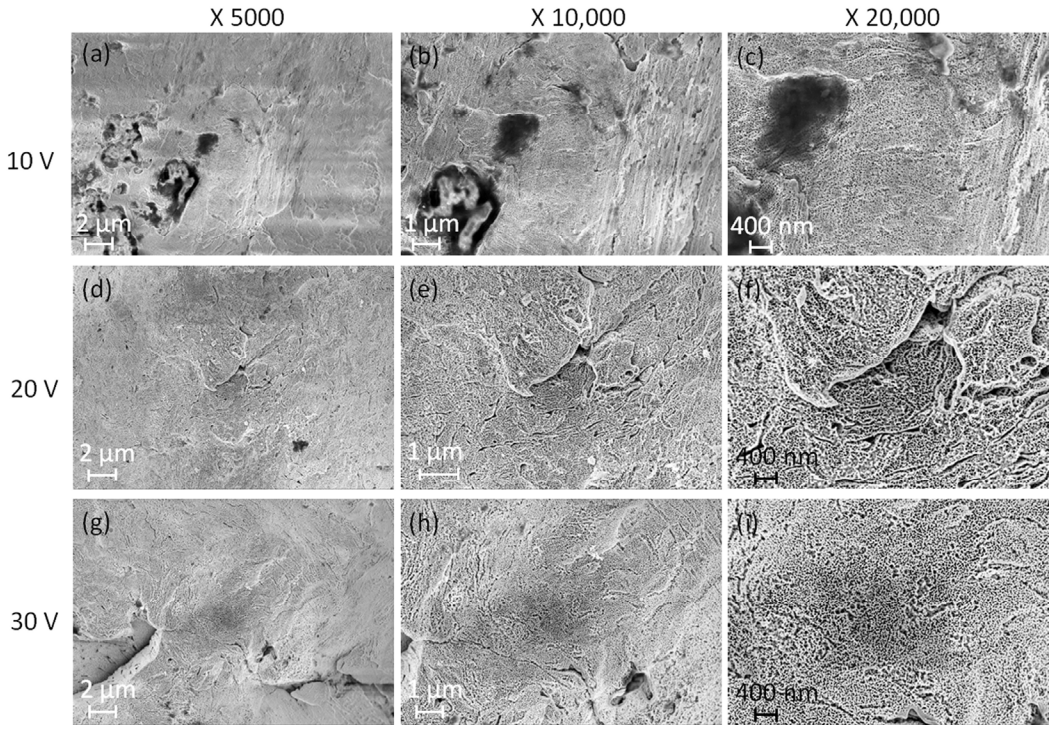

Figure 2. Comparison of the HRFESEM micrographs of Ti6Al4V coupons anodized at: (**a**–**c**) 10 V, (**d**–**f**) 20 V, and (**g**–**i**) 30 V during 4000 s in 1 M de $(NH_4)_2SO_4$ and 0.2% (w) NH_4F. Magnification: (**a**,**d**,**g**) ×5000, (**b**,**e**,**h**) ×10,000, (**c**,**f**,**i**) ×20,000.

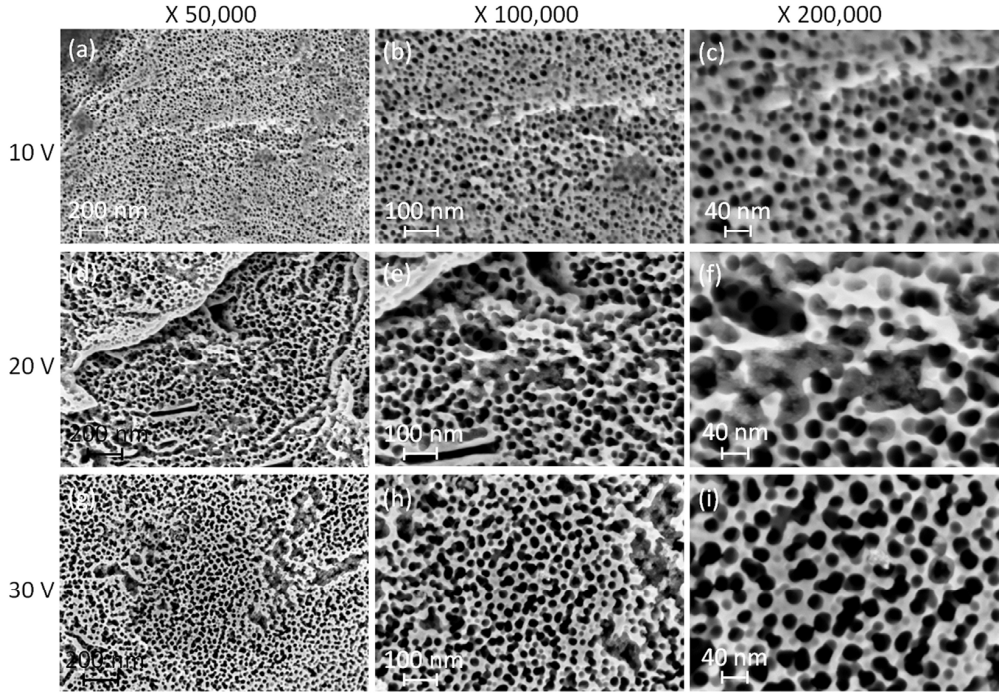

Figure 3. Comparison of the HRFESEM micrographs of Ti6Al4V coupons anodized at: (**a**–**c**) 10 V, (**d**–**f**) 20 V, and (**g**–**i**) 30 V during 4000 s in 1 M de $(NH_4)_2SO_4$ and 0.2% (w) NH_4F. Magnification: (**a**,**d**,**g**) ×50,000, (**b**,**e**,**h**) ×100,000, (**c**,**f**,**i**) ×200,000.

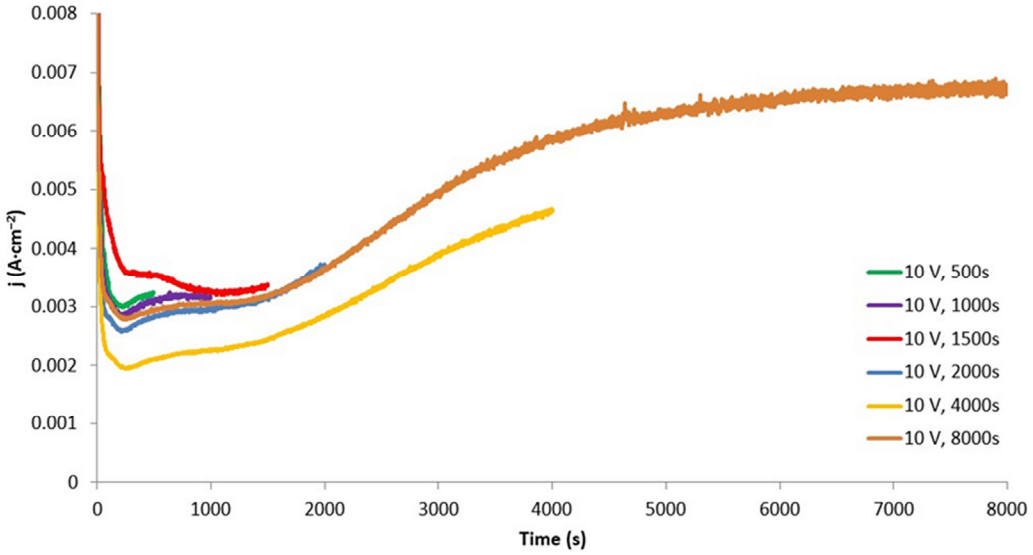

Figure 4. Chronoamperograms of the anodization of Ti6Al4V coupons obtained by additive manufacturing. Anodization potential: 10 V; anodization times: 500 s, 1000 s, 1500 s, 2000 s, 4000 s, and 8000 s; medium: 0.2% NH_4F and 1 M $(NH_4)_2SO_4$.

HRFESEM was used to evaluate the influence of synthesis time on the morphology of the anodized samples. In Figure 5, the HRFESEM micrographs for 2000 s, 4000 s, and 8000 s are compared. For 2000 s anodization (Figure 5a), some of the nanopores were not completely formed. For 4000 s of anodization (Figure 5b), the pores were completely formed as previously explained. For 8000 s (Figure 5c,d), the anodic layer grew three-dimensionally as the stabilization of the current density in the chronoamperogram of Figure 4 indicated, although the nanostructure obtained was not an ordered structure. For this reason, the optimal anodization time was 4000 s (equivalent to an electrical charge of 15 C). The conditions used in the anodization of the samples to be coated with AgNPs were 10 V of anodization potential and 15 C of electrical charge.

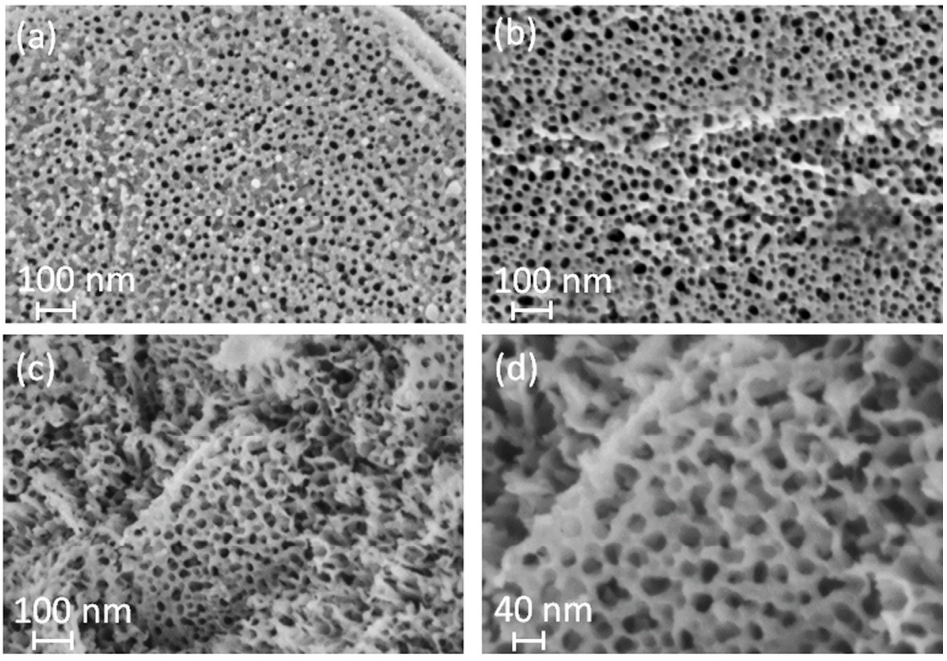

Figure 5. Comparison of the effect of anodization time: (**a**) 2000 s; (**b**) 4000 s, (**c**,**d**) 8000 s. Magnification: (**a**–**c**) ×100,000; (**d**) ×200,000.

3.2. Electrochemical Synthesis of AgNPs

The electrochemical synthesis of NPs involve methods that are widely applied in the literature [51,52] since they offer advantages such an easy control of the process, and the amount of nanomaterial deposited can be easily controlled by the electrical charge applied. Only two studies have previously conducted the electrochemical synthesis of AgNPs on anodized titanium [53,54]. Figure 6 shows the voltametric characterization of anodized Ti6Al4V coupons in a $[Ag(NH_3)_2]^+$ solution (0.05 M $AgNO_3$ + NH_4OH). In the first scan, a cathodic current density increase begins at around 0.1 V and continues until −0.5 V. This decrease can be attributed to the reduction of Ag^+ to Ag^0. In the following scans, a resistive behavior can be observed, which can be attributed to sluggish electron transfer derived from the poor conductivity of the anodized layer. From the first voltammogram, 0.1 V, 0.05 V, and 0 V potentials were selected to carry out the potentiostatic synthesis of AgNPs.

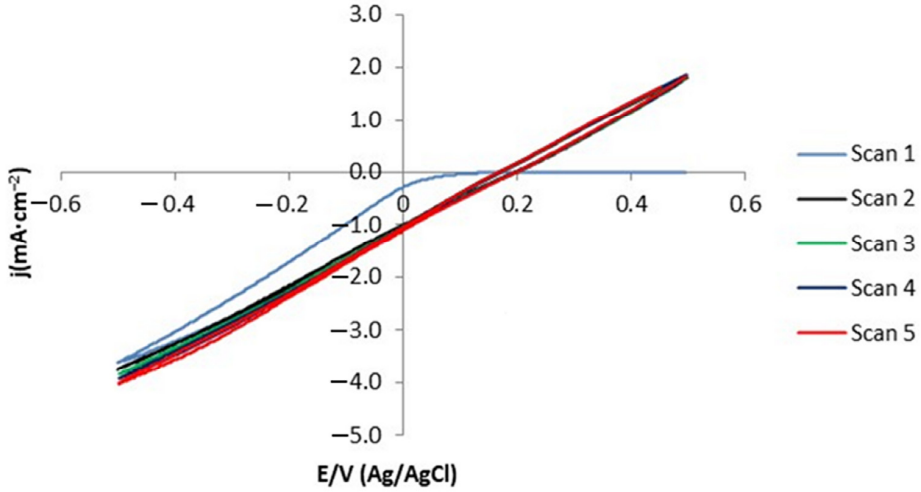

Figure 6. The cyclic voltammetry characterization of anodized Ti6Al4V coupons in a $[Ag(NH_3)_2]^+$ solution (0.05 M $AgNO_3$ + NH_4OH). Scan range: 0.5 V to −0.5 V. Scan rate: 50 $mV \cdot s^{-1}$.

Figure 7 shows the chronoamperograms of the synthesis of AgNPs on anodized Ti6Al4V coupons. As can be seen, the highest synthesis potential needed more time to achieve the electrical charge of 0.1 C due to the lowest current densities obtained at this potential. On the other hand, at 0 V, the synthesis time was the lowest due to the highest current density obtained.

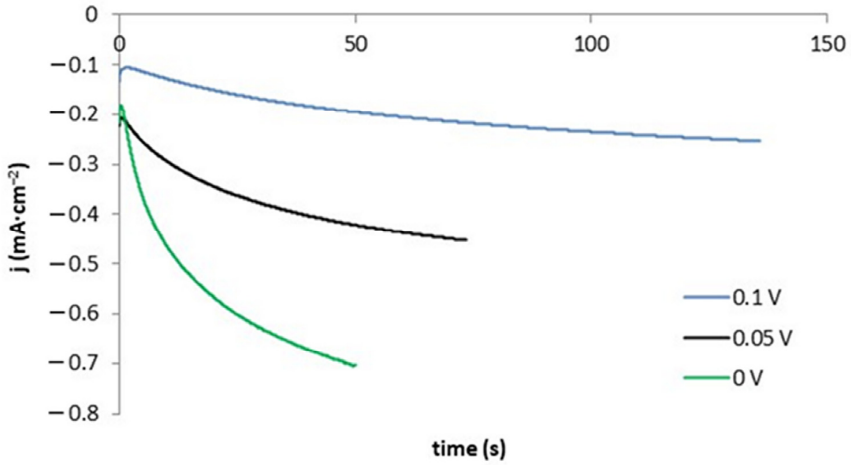

Figure 7. The chronoamperograms of the synthesis of AgNPs on anodized Ti6Al4V coupons in a $[Ag(NH_3)_2]^+$ solution (0.05 M $AgNO_3$ + NH_4OH). Synthesis potentials: 0 V, 0.05 V, 0.1 V. Synthesis charge: −0.1 C.

The theoretical amount of Ag deposited ($\mu g \cdot cm^{-2}$) was calculated by the synthesis charge ($C \cdot cm^{-2}$) (measured by the potentiostat/galvanostat), assuming that the only process that takes place is the reduction of Ag^+ to Ag^0 with a 100% efficiency [55]. The quantity of Ag ($m_{Ag/}cm^2$) was calculated according to Equation (3):

$$m_{Ag} = \frac{Q_{Ag} \cdot M}{4 \cdot F} \quad (3)$$

where Q_{Ag} is the synthesis charge (0.0271 $C \cdot cm^{-2}$); M is the Ag atomic weight (107.87 $g \cdot mol^{-1}$); 1 is the number of electrons involved in the reduction of Ag^+ to Ag^0; and F is the Faraday constant (96,485.3 $C \cdot mol^{-1}$). The calculated Ag load is around 30 $\mu g \cdot cm^{-2}$.

Figure 8 shows the micrographs obtained from the anodized coupons coated with AgNPs synthesized at different potentials. The micrographs were obtained with a backscatter electron detector, where higher atomic elements backscatter more electrons and appear as whiter zones in the micrographs. AgNPs appear as whither zones due to the higher atomic weight of Ag when compared to Ti, Al, V, and O, and AgNP distribution can be easily determined. Figure 8a,b shows the micrographs for the electrochemical synthesis of AgNPs carried out at 0.1 V. A good distribution of AgNPs was observed at a low magnification (Figure 8a) over the anodized surface, with nanoparticle size below 100 nm in general. At a high magnification, AgNPs were scarce (Figure 8b). When the potential of synthesis decreased to 0.05 V (Figure 8c,d), fewer nanoparticles were observed on the anodized surface. When the synthesis potential was further decreased to 0 V, a lower amount of AgNPs was observed, and their size increased (Figure 8e,f).

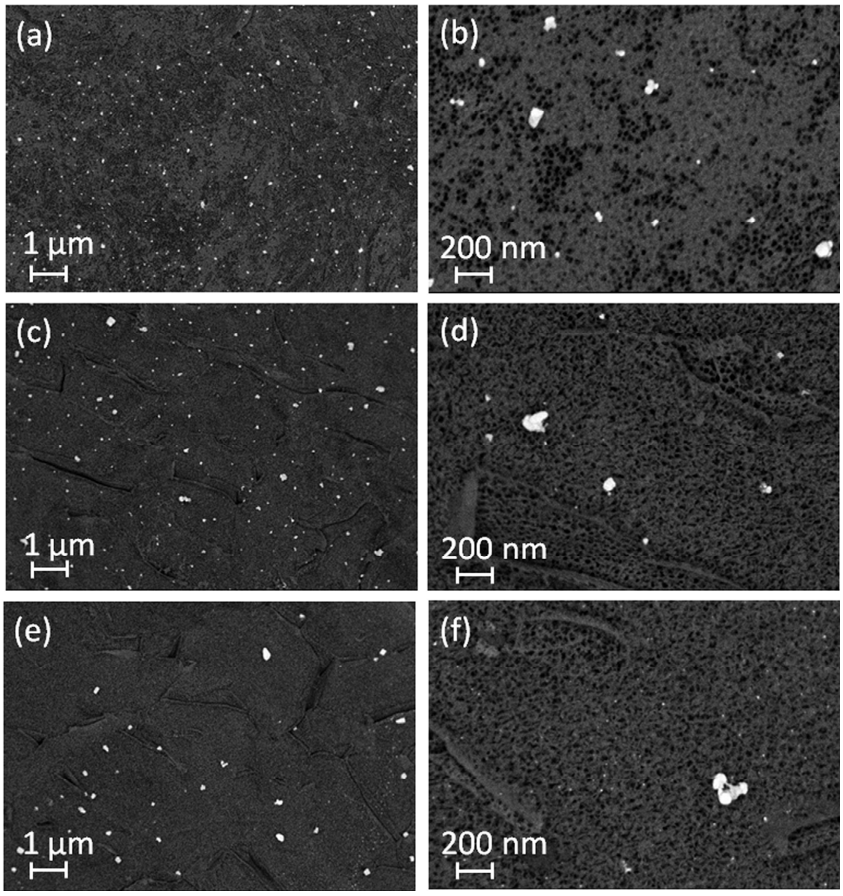

Figure 8. HRFESEM micrographs of Ti6Al4V coupons anodized at 10 V and coated with AgNPs synthesized electrochemically at: (**a**,**b**) 0.1 V, (**c**,**d**) 0.05 V, and (**e**,**f**) 0 V. Magnification: (**a**,**c**,**e**) ×10,000, (**b**,**d**,**f**) ×50,000. Micrographs obtained with backscatter electron detector.

In the case of the synthesis carried out at 0.1 V, AgNPs with geometrical three-dimensional forms appeared, as can be seen in Figure 9.

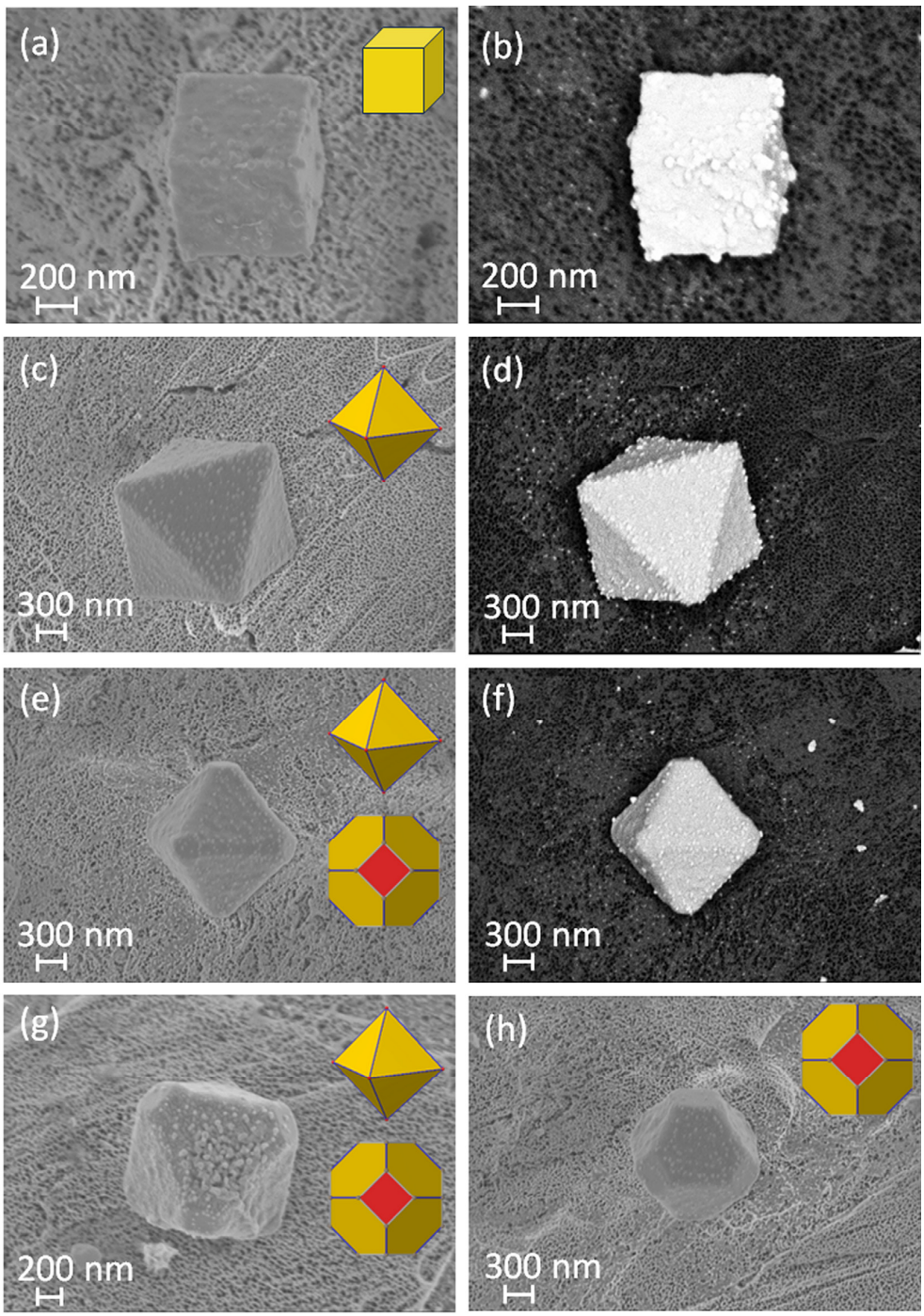

Figure 9. HRFESEM micrographs of Ti6Al4V coupons anodized at 10 V and coated with AgNPs synthesized electrochemically at: 0.1 V. Magnification: (**a**,**b**) ×50,000, (**c**–**f**) ×25,000, (**g**) ×31,970, (**h**) ×25,000. Micrographs obtained with: (**a**,**c**,**e**,**g**,**h**) in-Lens detector and (**b**,**d**,**f**) backscatter electron detector.

Cubic nanoparticles (Figure 9a,b), octahedron (Figure 9c,d), slightly truncated octahedron (Figure 9e–g), and fully truncated octahedron (face square) (Figure 9h) were observed. These morphologies have been obtained for chemically synthesized AgNPs [56], but have not been reported to be grown electrochemically to the best of our knowledge.

The formation of these geometric figures can be attributed to two factors. On one hand, the kinetics of the growth of the AgNPs at 0.1 V (low current density, as shown in Figure 7a) are slow, which allow for an arrangement of the atoms in these geometric forms. The other contributing factor is the poor conductivity of the anodized surface. Once AgNPs begin to be formed, it seems easier to continue the growth of these nanoparticles rather than creating new nucleation points, contributing to the growth of the single crystals [57]. Figure 9b,d,f shows the micrographs obtained with a backscatter electron detector to demonstrate that such polyhedron forms consist of Ag. The polyhedrons appear as white zones, which indicate that they are made from Ag. In addition, some dispersed AgNPs can also be observed on the surface of the anodized coupons.

3.3. Thermal Synthesis of AgNPs

A thermal method of the synthesis of AgNPs was also used, which has the advantage that both the TiO_2 recrystallization and AgNP deposition can be performed in one step. The temperature of 550 °C was selected as it is sufficient to produce the thermal reduction of Ag^+ to Ag^0 when the $AgNO_3$ precursor is used [58,59]. $AgNO_3$ typically decomposes at 444 °C [59]; in the present study, ammoniacal Ag was used, but the temperature of 550 °C was sufficient to produce the thermal reduction in Ag^+.

Figure 10 shows the micrographs of the anodized surface and was coated with AgNPs which were synthesized thermally. Backscattered electron micrographs allow for the easy location and distribution of AgNPs. At a low magnification (×10,000, ×20,000), only bigger Ag clusters can be observed (Figure 10a,b). At an intermediate magnification (×50,000, ×100,000), both the clusters and AgNPs can be observed (Figure 10c,d). At a high magnification (×200,000, ×300,000), the size of AgNPs can be observed. The size obtained is in general below 10 nm, which demonstrates the appropriateness of the thermal method for obtaining AgNPs of small size and which are well dispersed on the surface of anodized Ti6Al4V. However, the nanotube structure cannot be observed. The thermal treatment has probably produced a growth of the TiO_2 layer as observed. In future studies, the temperature should be optimized so that this layer does not excessively grow and cover the TiO_2 nanotubes. Removing the nanotubes would be detrimental, since these kinds of nanostructures favor osteointegration [60].

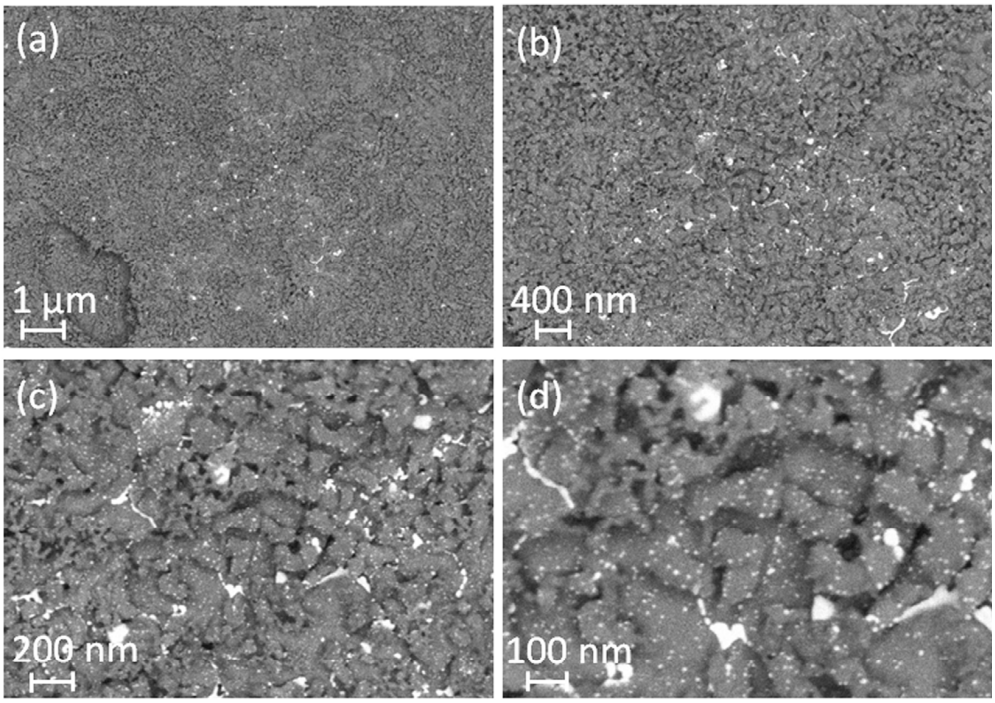

Figure 10. *Cont.*

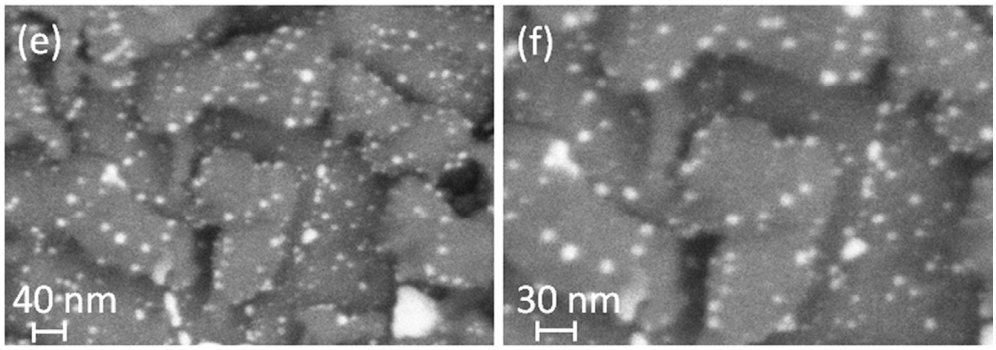

Figure 10. HRFESEM micrographs of Ti6Al4V coupons anodized at 10 V and coated with thermally synthesized AgNPs. Magnification: (**a**) ×10,000; (**b**) ×20,000; (**c**) ×50,000; (**d**) ×100,000; (**e**) ×200,000; (**f**) ×300,000. Micrographs obtained with a backscatter electron detector.

3.4. Chemical Synthesis of AgNPs

A chemical method of synthesis was also applied for obtaining AgNPs, where ammoniacal silver was previously adsorbed for 30 min on the Ti6Al4V coupons. After this time, the coupons were immersed in $NaBH_4$ to produce the formation of AgNPs due to the formation of reductive hydrogen during the process. Experimentally, it could be observed that some AgNPs were formed in the solution, and were aggregated and floated in the solution. Figure 11 shows the micrographs of the coatings obtained, where the AgNPs of a small size could be observed. At a medium magnification (Figure 11a,b), a good distribution of AgNPs was observed. At a high magnification (Figure 11c,d), AgNPs below 5 nm could be observed, although some bigger NPs could be also seen.

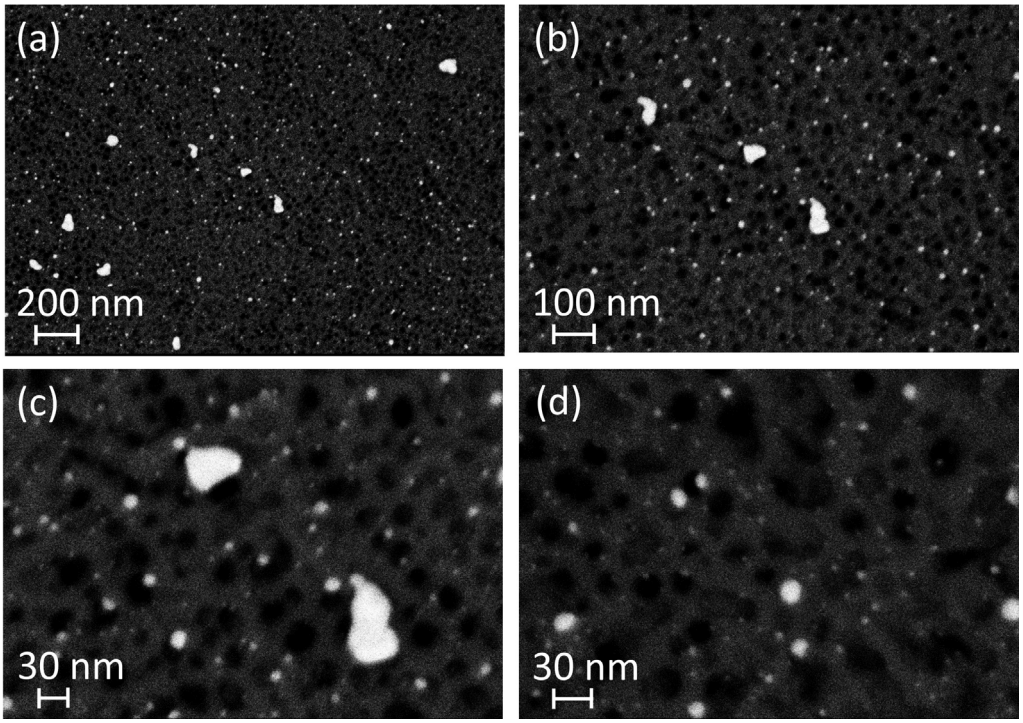

Figure 11. HRFESEM micrographs of Ti6Al4V coupons anodized at 10 V and coated with chemically synthesized AgNPs (drying step was not applied). Magnification: (**a**) ×50,000; (**b**) ×100,000; (**c**) ×250,000; (**d**) ×300,000. Micrographs obtained with a backscatter electron detector.

A second method of synthesis was employed, where, after the adsorption of ammoniacal silver, the coupons were extracted from the solution and were allowed to dry, and

finally, the Ag^+ was reduced to Ag^0 by $NaBH_4$ reduction. Figure 12 shows the micrographs of the anodized samples which were coated with AgNPs using this method. At a low magnification, the distribution observed was homogeneous, as can be seen in Figure 12a,b, where lots of AgNPs were observed. At a medium magnification (Figure 12c,d), both the TiO_2 nanotubes (black zones) and the AgNPs (white zones) can be easily distinguished. At a high magnification (Figure 12e,f), it can be seen that the size of the AgNPs is around 20–40 nm. The AgNPs are in general located over the anodized surface. The drying step seems to produce the joint of ammoniacal silver spots when the solvent is evaporated, thus increasing the size of the AgNPs when reduction is applied. Thus, the application of this stage (or not) produces a variation in the AgNPs' size.

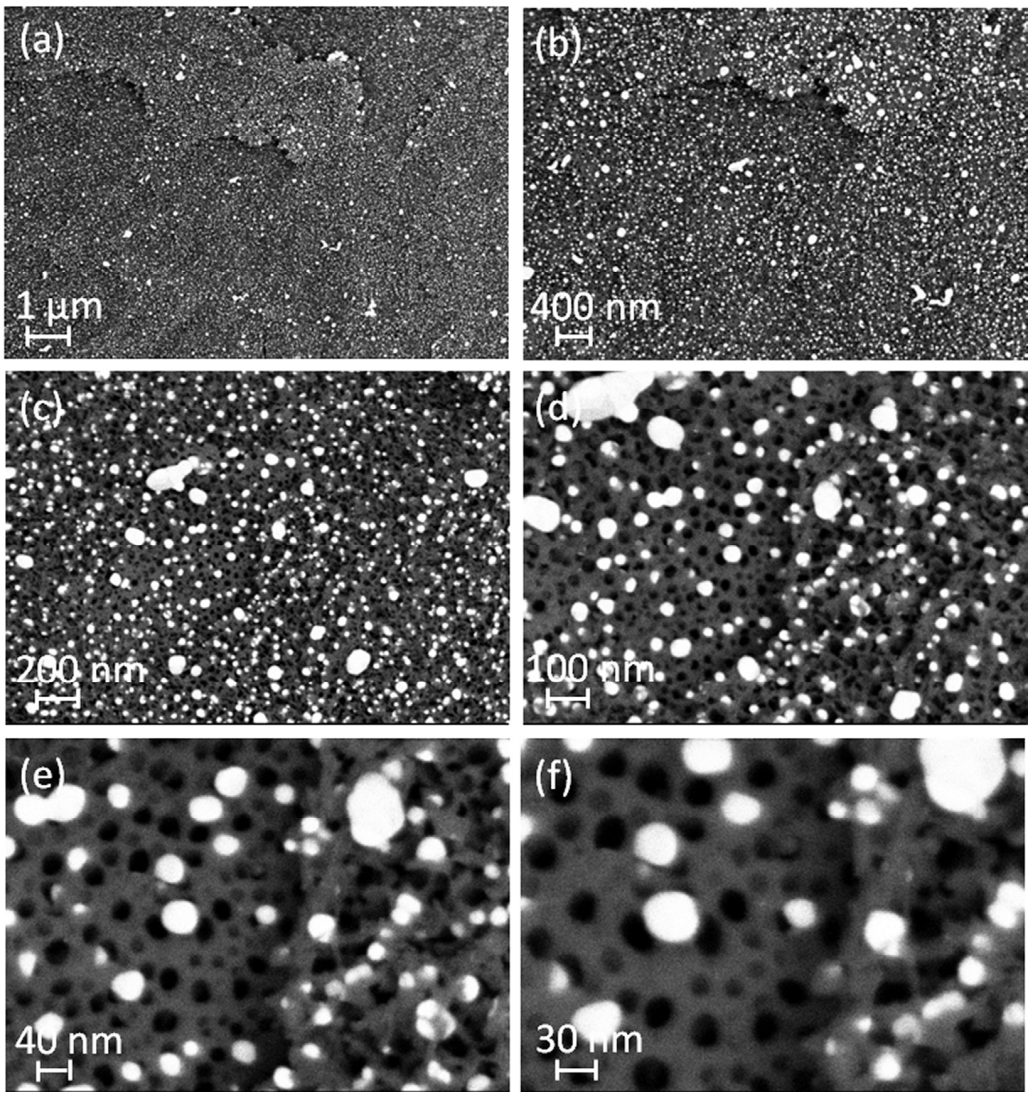

Figure 12. HRFESEM micrographs of Ti6Al4V coupons anodized at 10 V and coated with chemically synthesized AgNPs (drying step applied). Magnification: (**a**) ×10,000; (**b**) ×20,000; (**c**) ×50,000; (**d**) ×100,000; (**e**) ×200,000; (**f**) ×300,000. Micrographs obtained with a backscatter electron detector.

A reduction in the size of the AgNPs can be detrimental since it could produce cytotoxicity [61], as demonstrated in animals [62,63]. In the case of mice [63], it was demonstrated that AgNPs of around 10 nm had higher acute toxicity than bigger AgNPs (60 nm and 100 nm). This is why, for further studies, samples were coated using the method that includes the drying step.

Figure 13 shows a comparison of micrographs obtained at ×50,000 using the three methods for AgNPs synthesis. Comparing the three methods of synthesis, the chemical one produced a better coverage of the anodized surface and allowed for a better distribution of AgNPs while conserving the anodized structure. This is why this method was used to obtain antibacterial samples and study their Ag^+ release in SBF as well as their antibacterial performance against *S. aureus* V329 and *S. epidermidis* RP62A strains.

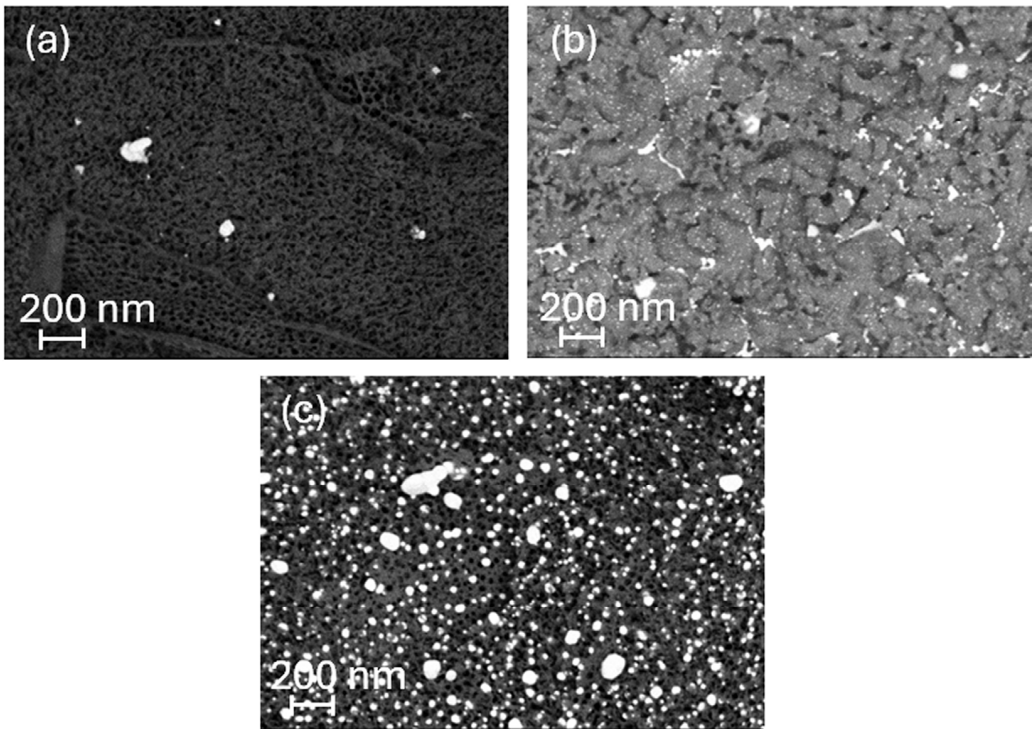

Figure 13. A comparison of the HRFESEM micrographs of Ti6Al4V coupons anodized at 10 V and coated with AgNPs synthesized (**a**) electrochemically, (**b**) thermally, (**c**) chemically (drying step applied). Magnification: ×50,000. Micrographs obtained with a backscatter electron detector.

3.5. Ag^+ Release Kinetics in SBF

One important aspect is the release kinetics of Ag^+ and its concentration (mg/L). Figure 14 shows the cumulated release of Ag^+ for 42 days as measured by ICP-MS. A Ag^+ release of 1.86 mg Ag^+/L was achieved within 42 days. In the first few days, where an infection after the implantation of a prosthetic device is most probable, the Ag^+ release was higher than in the following days. The concentration of Ag^+ released is not dangerous for human cells, since the potential toxic limit of Ag^+ is 10 mg/L [64,65].

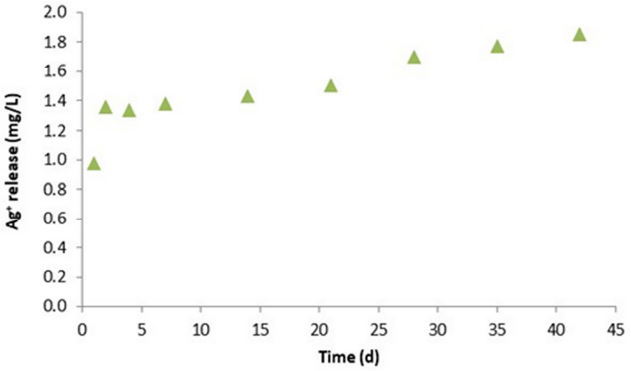

Figure 14. Temporal Ag^+ cumulated release (mg/L) for the anodized sample coated with chemically synthesized AgNPs.

3.6. Antibacterial Tests

To investigate the antibacterial capacity of anodized Ti6Al4V coated with chemically synthesized AgNPs, both *S. aureus* and *S. epidermidis* were chosen as model bacteria due to their close association with most orthopedic infections, and this was evaluated following ISO 22196 standard [44]. Figure 15 shows that the anodized Ti6Al4V + AgNP sample achieved a more than 7-log reduction in viable cells of both *S. aureus* and *S. epidermidis* after 24 h of exposure compared to the bare Ti6Al4V and anodized Ti6Al4V samples, which produced a lethality > 99.9% of *S. aureus* and *S. epidermidis*. A comparison was made using the *t*-test with R comparing the anodized Ti6Al4V + AgNPs with each control (Ti6Al4V and anodized Ti6Al4V samples, with a significant reduction in all cases ($p \leq 0.05$). Consequently, the anodized Ti6Al4V + AgNP sample demonstrates remarkable bactericidal activity against both bacterium strains.

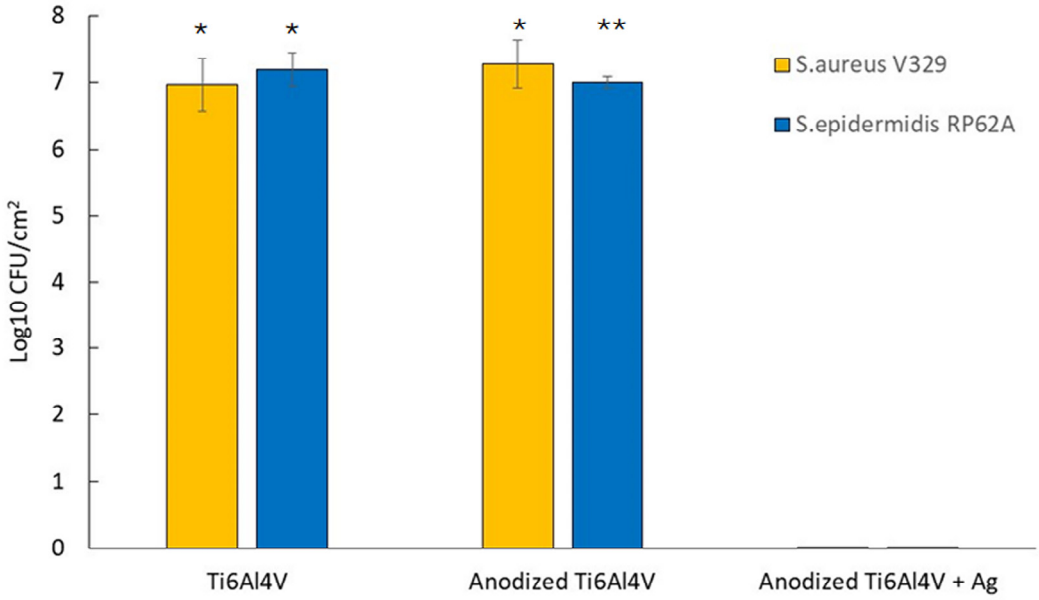

Figure 15. A comparison of bactericidal activity against the *S. aureus* V329 strain and *S. epidermidis* RP62A strain of different Ti6Al4V materials. The bars indicate the mean of Log10 (UFC/mL) and error bars correspond to standard deviation. The comparison is produced with *t*-test by matching anodized Ti6Al4V + AgNPs against the controls (Ti6Al4V and anodized Ti6Al4V). *: $p \leq 0.05$ and **: $p \leq 0.01$.

The ability of bacteria to attach to medical devices and host tissue is the first step in the subsequent generation of mature biofilms, leading to severe infections. Furthermore, biofilms enhance bacterial resistance to antibiotics and evade the host's immune system, making its removal from the implant surface challenging. Consequently, minimizing microbial adhesion has become a critical strategy for preventing infections associated with prosthetic implants [66].

Therefore, the ability of anodized Ti6Al4V + AgNPs to prevent biofilm formation was analyzed. Quantitatively, anodized Ti6Al4V + AgNPs exhibited robust efficacy in reducing biofilm formation after 48 h of incubation with both *S. aureus* and *S. epidermidis* strains (Figure 16). The anodized Ti6Al4V + AgNP sample demonstrated a remarkable 6-log reduction in the viable biofilm cells of *S. aureus* and *S. epidermidis* compared to Ti6Al4V and anodized Ti6Al4V (as shown in Figure 16). Moreover, the average lethality of *S. aureus* and *S. epidermidis* biofilm on the anodized Ti6Al4V + AgNPs material was >99.9% when compared to control groups (Ti6Al4V and anodized Ti6Al4V). A comparison was made using the *t*-test with R, comparing anodized Ti6Al4V + AgNPs with each control (Ti6Al4V and anodized Ti6Al4V samples, with a significant reduction in all cases ($p \leq 0.01$)). These findings highlight the strong biofilm prevention properties of anodized Ti6Al4V +

AgNPs, which could significantly mitigate ODRI risk by inhibiting biofilm formation on prosthetic devices.

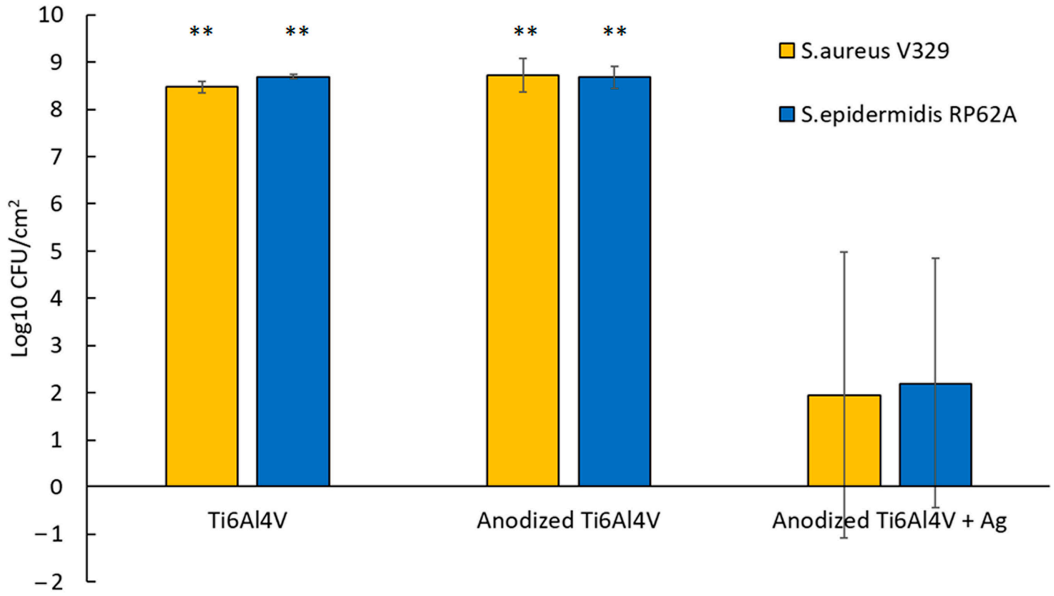

Figure 16. A comparison of the biofilm formation of the *S. aureus* V329 strain and *S. epidermidis* RP62A strain on different Ti6Al4V materials. The bars indicate the mean of Log10 (UFC/mL) and error bars correspond to standard deviation. The comparison is produced with *t*-test by matching anodized Ti6Al4V + AgNPs against the controls (Ti6Al4V and anodized Ti6Al4V). **: $p \leq 0.01$.

Personalized medicine has revolutionized healthcare by providing treatments that are adapted to individual patients. New requirements in medicine demand customized prosthetic implants that offer several benefits, including anatomical fit, improved functionality, and reduced postoperative complications [67]. In this perspective, the additive manufacturing of Ti6Al4V could be a promising solution in the field of prosthetic implants, enabling the fabrication of patient-specific implants. Moreover, these implants can be adapted to the patient's anatomy, improving both esthetics and function [68]. Furthermore, these new implants should be able to prevent future infections, e.g., through drug delivery [69]. The additively manufactured Ti6Al4V, anodized and coated with chemically deposited AgNPs, developed in this article fulfils all these requirements. It can be manufactured to be adapted to the needs of the patient and, in addition, we have demonstrated that this new surface-modified additively manufactured material has excellent bactericidal activity and is able to significantly reduce the biofilm formation of the most relevant species in ODRIs. This antibacterial effect may be due to the release of silver cations from the Ti6Al4V surface, as these cations disrupt the bacterial cell wall, induce DNA alterations, trigger the production of reactive oxygen species, and ultimately inactivate essential proteins [70].

4. Conclusions

A nanostructured layer of TiO_2 nanopores was obtained by the anodization of Ti6Al4V samples fabricated by additive manufacturing (electron beam melting). The optimal anodization conditions obtained in this work were 10 V and 4000 s. Higher anodization potentials (20 V and 30 V) produced the merging of individual pores. In the case of anodization time, shorter anodization times did not allow for the complete formation of the nanopores and longer anodization times produced an excessive growth of the TiO_2 layer.

Three methods of the synthesis of AgNPs were used in the study: electrochemical, thermal, and chemical. The electrochemical method was performed at different potentials (0.1 V, 0.05 V, and 0 V); however, not enough AgNPs were observed on the anodized surface by HRFESEM. The synthesis at 0.1 V showed the formation of cubic, octahedra,

and truncated octahedra Ag crystals due to the slow kinetic growth at this potential. The thermal method of synthesis showed a good distribution of AgNPs; however, the TiO_2 nanostructure was damaged, probably due to the temperature used. The chemical method of synthesis showed a good distribution of AgNPs and the maintenance of the TiO_2 nanostructure. The drying stage between the adsorption and the reduction by $NaBH_4$ also affected the size of the NPs obtained. The inclusion of the drying stage produced bigger AgNPs than when it was not used. Based on the microscopy analysis, the samples coated with chemically obtained AgNPs were selected to carry out further studies.

Ag^+ release was tested in simulated body fluid at 37 °C, and 1.86 mg Ag^+/L was obtained after 42 days of lixiviation, not reaching toxic limits for human cells. Antibacterial tests showed excellent bactericidal activity and inhibited biofilm formation for the *S. aureus V329* and *S. epidermidis* RP62A strains (lethality > 99.9% for both bacteria and assays).

The reported method stands out for its simplicity and homogeneous distribution of AgNPs over the Ti6Al4V surface and demonstrates its application for additively manufactured Ti6Al4V. Additive manufacturing is a promising solution in the field of prosthetic implants, enabling the fabrication of patient-specific implants which adapt to the patient's anatomy, improving esthetics and functionality. The nanopores created on the metal surface during anodizing could also be used as nanocontainers, where differing antibacterial agents can be stored and released with the aid of stimuli-responsive molecular gates.

Author Contributions: Conceptualization, J.M.; methodology, J.M., A.V.-G., M.Á.T.-M. and F.B.; investigation, J.M., A.V.-G., P.B.-Q., M.Á.T.-M. and F.B.; data curation, J.M. and M.Á.T.-M.; writing—original draft preparation, J.M.; writing—review and editing, J.M., A.V.-G., P.B.-Q., M.Á.T.-M. and F.B.; visualization, J.M.; supervision, J.M. and F.B.; project administration, J.M.; funding acquisition, J.M. All authors have read and agreed to the published version of the manuscript.

Funding: This research was funded by the Instituto Valenciano de Competitividad Empresarial (IVACE), grant number IMDEEA/2020/33, and the European Union (FEDER).

Data Availability Statement: The raw data supporting the conclusions of this article will be made available by the authors on request.

Acknowledgments: Jessica Belda is gratefully acknowledged for carrying out ICP-MS measurements. The Electron Microscopy Service of the UPV (Universitat Politècnica de València) is gratefully acknowledged for help with HRFESEM.

Conflicts of Interest: The authors declare no conflicts of interest.

References

1. Ngo, T.D.; Kashani, A.; Imbalzano, G.; Nguyen, K.T.Q.; Hui, D. Additive manufacturing (3D printing): A review of materials, methods, applications and challenges. *Compos. Part-B-Eng.* **2018**, *143*, 172–196. [CrossRef]
2. Yaragatti, N.; Patnaik, A. A review on additive manufacturing of polymers composites. *Mater. Today Proc.* **2021**, *44*, 4150–4157. [CrossRef]
3. Gorsse, S.; Hutchinson, C.; Gouné, M.; Banerjee, R. Additive manufacturing of metals: A brief review of the characteristic microstructures and properties of steels, Ti-6Al-4V and high-entropy alloys. *Sci. Technol. Adv. Mat.* **2017**, *18*, 584–610. [CrossRef] [PubMed]
4. Zocca, A.; Colombo, P.; Gomes, C.M.; Günster, J. Additive Manufacturing of Ceramics: Issues, Potentialities, and Opportunities. *J. Am. Ceram. Soc.* **2015**, *98*, 1983–2001. [CrossRef]
5. Paolini, A.; Kollmannsberger, S.; Rank, E. Additive manufacturing in construction: A review on processes, applications, and digital planning methods. *Addit. Manuf.* **2019**, *30*, 100894. [CrossRef]
6. Tomec, D.K.; Karič, M. Use of Wood in Additive Manufacturing: Review and Future Prospects. *Polymers* **2022**, *14*, 1174. [CrossRef] [PubMed]
7. Liu, S.; Shin, Y.C. Additive manufacturing of Ti6Al4V alloy: A review. *Mater. Des.* **2019**, *164*, 107552. [CrossRef]
8. Calderón, L.A.Á.; Graf, B.; Rehmer, B.; Petrat, T.; Skrotzki, B.; Rethmeier, M. Characterization of Ti–6Al–4V Fabricated by Multilayer Laser Powder-Based Directed Energy Deposition. *Adv. Eng. Mater.* **2022**, *24*, 2101333. [CrossRef]
9. Aufa, A.N.; Hassan, M.Z.; Ismail, Z. Recent advances in Ti-6Al-4V additively manufactured by selective laser melting for biomedical implants: Prospect development. *J. Alloys Compd.* **2022**, *896*, 163072. [CrossRef]
10. Kolamroudi, M.K.; Asmael, M.; Ilkan, M.; Kordani, N. Developments on Electron Beam Melting (EBM) of Ti–6Al–4V: A Review. *Trans. Indian Inst. Met.* **2021**, *74*, 783–790. [CrossRef]

11. Koju, N.; Niraula, S.; Fotovvati, B. Additively Manufactured Porous Ti6Al4V for Bone Implants: A Review. *Metals* **2022**, *12*, 687. [CrossRef]
12. Harun, W.S.W.; Manam, N.S.; Kamariah, M.S.I.N.; Sharif, S.; Zulkifly, A.H.; Ahmad, I.; Miura, H. A review of powdered additive manufacturing techniques for Ti-6al-4v biomedical applications. *Powder Technol.* **2018**, *331*, 74–97. [CrossRef]
13. Bandekhoda, M.R.; Mosallanejad, M.H.; Atapour, M.; Iuliano, L.; Saboori, A. Investigation on the Potential of Laser and Electron Beam Additively Manufactured Ti–6Al–4V Components for Orthopedic Applications. *Met. Mater. Int.* **2024**, *30*, 114–126. [CrossRef]
14. Demirci, S.; Dalmış, R.; Dikici, T.; Tünçay, M.M.; Kaya, N.; Güllüoğlu, A.N. Effect of surface modifications of additively manufactured Ti-6Al-4V alloys on apatite formation ability for biomedical applications. *J. Alloys Compd.* **2021**, *887*, 161445. [CrossRef]
15. Demirci, S.; Dikici, T.; Tünçay, M.M.; Dalmış, R.; Kaya, N.; Kanbur, K.; Sargin, F.; Güllüoğlu, A.N. Investigation of surface-modified EBM printed Ti-6Al-4V alloys for biomedical applications. *Surf. Interfaces* **2022**, *34*, 102372. [CrossRef]
16. Rasouli, R.; Barhoum, A.; Uludag, H. A review of nanostructured surfaces and materials for dental implants: Surface coating, patterning and functionalization for improved performance. *Biomater. Sci.* **2018**, *6*, 1312–1338. [CrossRef] [PubMed]
17. Thakali, A.; MacRae, J.D. A review of chemical and microbial contamination in food: What are the threats to a circular food system? *Environ. Res.* **2021**, *194*, 110635. [CrossRef] [PubMed]
18. Ferraris, S.; Spriano, S. Antibacterial titanium surfaces for medical implants. *Mater. Sci. Eng. C* **2016**, *61*, 965–978. [CrossRef] [PubMed]
19. Tande, A.J.; Patel, R. Prosthetic Joint Infection. *Clin. Microbiol. Rev.* **2014**, *27*, 302–345. [CrossRef]
20. Seidelman, J.L.; Mantyh, C.R.; Anderson, D.J. Surgical Site Infection Prevention A Review. *J. Am. Med. Assoc.* **2023**, *329*, 244–252. [CrossRef]
21. Shineh, G.; Mobaraki, M.; Bappy, M.J.P.; Mills, D.K. Biofilm Formation, and Related Impacts on Healthcare, Food Processing and Packaging, Industrial Manufacturing, Marine Industries, and Sanitation–A Review. *Appl. Microbiol.* **2023**, *3*, 629–665. [CrossRef]
22. Koehle, A.P.; Brumwell, S.L.; Seto, E.P.; Lynch, A.M.; Urbaniak, C. Microbial applications for sustainable space exploration beyond low Earth orbit. *npj Microgravity* **2023**, *9*, 47. [CrossRef]
23. Garrett, T.R.; Bhakoo, M.; Zhang, Z. Bacterial adhesion and biofilms on surfaces. *Prog. Nat. Sci.* **2008**, *18*, 1049–1056. [CrossRef]
24. Grinberg, M.; Orevi, T.; Kashtan, N. Bacterial surface colonization, preferential attachment and fitness under periodic stress. *PLoS Comput. Biol.* **2019**, *15*, e1006815. [CrossRef]
25. Basile, G.; Gallina, M.; Passeri, A.; Gaudio, R.M.; Castelnuovo, N.; Ferrante, P.; Calori, G.M. Prosthetic joint infections and legal disputes: A threat to the future of prosthetic orthopedics. *J. Orthop. Traumatol.* **2021**, *22*, 44. [CrossRef]
26. Kennedy, D.G.; O'Mahony, A.M.; Culligan, E.P.; O'Driscoll, C.M.; Ryan, K.B. Strategies to Mitigate and Treat Orthopaedic Device-Associated Infections. *Antibiotics* **2022**, *11*, 1822. [CrossRef]
27. Premkumar, A.; Kolin, D.A.; Farley, K.X.; Wilson, J.M.; McLawhorn, A.S.; Cross, M.B.; Sculco, P.K. Projected Economic Burden of Periprosthetic Joint Infection of the Hip and Knee in the United States. *J. Arthroplasty* **2021**, *36*, 1484–1489. [CrossRef]
28. Vavasseur, B.L.; Zeller, V. Antibiotic Therapy for Prosthetic Joint Infections: An Overview. *Antibiotics* **2022**, *11*, 486. [CrossRef]
29. Gómez-Junyent, J.; Lora-Tamayo, J.; Baraia-Etxaburu, J.; Sánchez-Somolinos, M.; Iribarren, J.A.; Rodriguez-Pardo, D.; Praena-Segovia, J.; Sorlí, L.; Bahamonde, A.; Rier, M.; et al. Implant Removal in the Management of Prosthetic Joint Infection by Staphylococcus aureus: Outcome and Predictors of Failure in a Large Retrospective Multicenter Study. *Antibiotics* **2021**, *10*, 118. [CrossRef] [PubMed]
30. Shree, P.; Singh, C.K.; Sodhi, K.K.; Surya, J.N.; Singh, D.K. Biofilms: Understanding the structure and contribution towards bacterial resistance in antibiotics. *Med. Microecol.* **2023**, *16*, 100084. [CrossRef]
31. Getzlaf, M.A.; Lewallen, E.A.; Kremers, H.M.; Jones, D.L.; Bonin, C.A.; Dudakovic, A.; Thaler, R.; Cohen, R.C.; Lewallen, D.G.; Wijnen, A.J.v. Multi-disciplinary antimicrobial strategies for improving orthopaedic implants to prevent prosthetic joint infections in hip and knee. *J. Orthop. Res.* **2016**, *34*, 177–186. [CrossRef] [PubMed]
32. Li, B.; Webster, T.J. Bacteria Antibiotic Resistance: New Challenges and Opportunities for Implant-Associated Orthopedic Infections. *J. Orthop. Res.* **2018**, *36*, 22–32. [CrossRef] [PubMed]
33. Cloutier, M.; Mantovani, D.; Rosei, F. Antibacterial Coatings: Challenges, Perspectives, and Opportunities. *Trends Biotechnol.* **2015**, *33*, 637–652. [CrossRef] [PubMed]
34. Lemire, J.A.; Harrison, J.J.; Turner, R.J. Antimicrobial activity of metals: Mechanisms, molecular targets and applications. *Nat. Rev. Microbiol.* **2013**, *11*, 371–384. [CrossRef] [PubMed]
35. Jakubowski, M.; Voelkel, A.; Sandomierski, M. Crystalline Zeolite Layers on the Surface of Titanium Alloys in Biomedical Applications: Current Knowledge and Possible Directions of Development. *Crystals* **2022**, *12*, 1520. [CrossRef]
36. Wang, F.; Li, C.; Zhang, S.; Liu, H. Role of TiO_2 Nanotubes on the Surface of Implants in Osseointegration in Animal Models: A Systematic Review and Meta-Analysis. *J. Prosthodont.* **2020**, *29*, 501–510. [CrossRef] [PubMed]
37. Ren, B.; Wan, Y.; Liu, C.; Wang, H.; Yu, M.; Zhang, X.; Huang, Y. Improved osseointegration of 3D printed Ti-6Al-4V implant with a hierarchical micro/nano surface topography: An in vitro and in vivo study. *Mater. Sci. Eng. C* **2021**, *118*, 111505. [CrossRef] [PubMed]

38. Ulfah, I.M.; Fitriani, D.A.; Azahra, S.A.; Saudi, A.U.; Kozin, M.; Hanafi, R.; Puranto, P.; Damisih; Sugeng, B.; Thaha, Y.N.; et al. Effect of cathode material on the morphology and osseointegration of TiO_2 nanotube arrays by electrochemical anodization technique. *Surf. Coat. Technol.* **2023**, *470*, 129836. [CrossRef]
39. Jiang, P.; Zhang, Y.; Hu, R.; Wang, X.; Lai, Y.; Rui, G.; Lin, C. Hydroxyapatite-modified micro/nanostructured titania surfaces with different crystalline phases for osteoblast regulation. *Bioact. Mater.* **2021**, *6*, 1118–1129. [CrossRef]
40. Qin, J.; Yang, D.; Maher, S.; Lima-Marques, L.; Zhou, Y.; Chen, Y.; Atkins, G.J.; Losic, D. Micro- and nano-structured 3D printed titanium implants with a hydroxyapatite coating for improved osseointegration. *J. Mater. Chem. B* **2018**, *6*, 3136–3144. [CrossRef]
41. Dong, J.; Chen, F.; Yao, Y.; Wu, C.; Ye, S.; Ma, Z.; Yuan, H.; Shao, D.; Wang, L.; Wang, Y. Bioactive mesoporous silica nanoparticle-functionalized titanium implants with controllable antimicrobial peptide release potentiate the regulation of inflammation and osseointegration. *Biomaterials* **2024**, *305*, 122465. [CrossRef] [PubMed]
42. Lyons, J.G.; Plantz, M.A.; Hsu, W.K.; Hsu, E.L.; Minardi, S. Nanostructured Biomaterials for Bone Regeneration. *Front. Bioeng. Biotechnol.* **2020**, *8*, 922. [CrossRef] [PubMed]
43. Kokubo, T.; Kushitani, H.; Sakka, S.; Kitsugi, T.; Yamamuro, T. Solutions able to reproduce in vivo surface-structure changes in bioactive glass-ceramic A-W. *J. Biomed. Mater. Res.* **1990**, *24*, 721–734. [CrossRef]
44. *ISO 22196*; Measurement of Antibacterial Activity on Plastics and Other Non-Porous Surfaces. ISO: Geneva, Switzerland, 2011.
45. Beranek, R.; Hildebrand, H.; Schmuki, P. Self-Organized Porous Titanium Oxide Prepared in H_2SO_4/HF Electrolytes. *Electrochem. Solid-State Lett.* **2003**, *6*, B12–B14. [CrossRef]
46. Smith, Y.R.; Ray, R.S.; Carlson, K.; Sarma, B.; Misra, M. Self-Ordered Titanium Dioxide Nanotube Arrays: Anodic Synthesis and Their Photo/Electro-Catalytic Applications. *Materials* **2013**, *6*, 2892–2957. [CrossRef]
47. Warczak, M.; Sadkowski, A. Oscillatory regime of titanium anodization under voltage control. *Electrochem. Commun.* **2009**, *11*, 1733–1735. [CrossRef]
48. Molina, J.; Valero-Gómez, A.; Belda, J.; Bosch, F.; Bernabé-Quispe, P.; Tormo-Mas, M.A. Long-term antibacterial Ag^+-release biomaterials based on anodized Ti6Al4V and silver nanoparticles. *Colloids Surf. A Physicochem. Eng. Asp.* **2023**, *676*, 132243. [CrossRef]
49. Saha, S.K.; Park, Y.J.; Cho, S.O. Fabrication of highly ordered nanoporous oxide layer on Ti6Al4V surfaces for improved corrosion resistance property. *J. Mol. Struct.* **2021**, *1223*, 129244. [CrossRef]
50. Goddeti, K.C.; Lee, C.; Lee, Y.K.; Park, J.Y. Three-dimensional hot electron photovoltaic device with vertically aligned TiO_2 nanotubes. *Sci. Rep.* **2018**, *8*, 7330. [CrossRef]
51. Petrii, O.A. Electrosynthesis of nanostructures and nanomaterials. *Russ. Chem. Rev.* **2015**, *84*, 159–193. [CrossRef]
52. Li, G.-R.; Xu, H.; Lu, X.-F.; Feng, J.-X.; Tong, Y.-X.; Su, C.-Y. Electrochemical synthesis of nanostructured materials for electrochemical energy conversion and storage. *Nanoscale* **2013**, *5*, 4056–4069. [CrossRef] [PubMed]
53. Durdu, S.; Yalçin, E.; Altinkök, A.; Çavuşoğlu, K. Characterization and investigation of electrochemical and biological properties of antibacterial silver nanoparticle-deposited TiO_2 nanotube array surfaces. *Sci. Rep.* **2023**, *13*, 4699. [CrossRef] [PubMed]
54. Godoy-Gallardo, M.; Rodríguez-Hernández, A.G.; Delgado, L.M.; Manero, J.M.; Gil, F.J.; Rodríguez, D. Silver deposition on titanium surface by electrochemical anodizing process reduces bacterial adhesion of *Streptococcus sanguinis* and *Lactobacillus salivarius*. *Clin. Oral Impl. Res.* **2015**, *26*, 1170–1179. [CrossRef]
55. Molina, J.; Fernández, J.; del Río, A.I.; Bonastre, J.; Cases, F. Characterization of azo dyes on Pt and Pt/polyaniline/dispersed Pt electrodes. *Appl. Surf. Sci.* **2012**, *258*, 6246–6256. [CrossRef]
56. Xia, Y.; Xiong, Y.; Lim, B.; Skrabalak, S.E. Shape-Controlled Synthesis of Metal Nanocrystals: Simple Chemistry Meets Complex Physics? *Angew. Chem. Int. Ed.* **2009**, *48*, 60–103. [CrossRef] [PubMed]
57. An, K.; Somorjai, G.A. Size and Shape Control of Metal Nanoparticles for Reaction Selectivity in Catalysis. *ChemCatChem* **2012**, *4*, 1512–1524. [CrossRef]
58. Yu, B.; Leung, K.M.; Guo, Q.; Lau, W.M.; Yang, J. Synthesis of Ag–TiO_2 composite nano thin film for antimicrobial application. *Nanotechnology* **2011**, *22*, 115603. [CrossRef]
59. Qu, J.; Lu, X.; Li, D.; Ding, Y.; Leng, Y.; Weng, J.; Qu, S.; Feng, B.; Watari, F. Silver/hydroxyapatite composite coatings on porous titanium surfaces by sol-gel method. *J. Biomed. Mater. Res. B* **2011**, *97B*, 40–48. [CrossRef]
60. Jarosz, M.; Grudzień, J.; Kapusta-Kołodziej, J.; Chudecka, A.; Sołtys, M.; Sulka, G.D. Anodizing of titanium alloys for biomedical applications. In *Nanostructured Anodic Metal Oxides Synthesis and Applications*; Sulka, G.D., Ed.; Elsevier: Amsterdam, The Netherlands, 2020; pp. 211–275. [CrossRef]
61. Liao, C.; Li, Y.; Tjong, S.C. Bactericidal and Cytotoxic Properties of Silver Nanoparticles. *Int. J. Mol. Sci.* **2019**, *20*, 449. [CrossRef]
62. Nie, P.; Zhao, Y.; Xu, H. Synthesis, applications, toxicity and toxicity mechanisms of silver nanoparticles: A review. *Ecotoxicol. Environ. Saf.* **2023**, *253*, 114636. [CrossRef]
63. Cho, Y.-M.; Mizuta, Y.; Akagi, J.-i.; Toyoda, T.; Sone, M.; Ogawa, K. Size-dependent acute toxicity of silver nanoparticles in mice. *J. Toxicol. Pathol.* **2018**, *31*, 73–80. [CrossRef] [PubMed]
64. Guo, Z.; Chen, C.; Gao, Q.; Li, Y.; Zhang, L. Fabrication of silver-incorporated TiO_2 nanotubes and evaluation on its antibacterial activity. *Mater. Lett.* **2014**, *137*, 464–467. [CrossRef]
65. Shivaram, A.; Bose, S.; Bandyopadhyay, A. Understanding long-term silver release from surface modified porous titanium implants. *Acta Biomater.* **2017**, *58*, 550–560. [CrossRef] [PubMed]

66. Master, E.A.; Ricciardi, B.F.; de Mesy Bentley, K.L.; Moriarty, T.F.; Schwarz, E.M.; Muthukrishnan, G. Skeletal infections: Microbial pathogenesis, immunity and clinical management. *Nat. Rev. Microbiol.* **2022**, *20*, 385–400. [CrossRef] [PubMed]
67. Kouhi, M.; Araújo, I.J.d.S.; Asa'ad, F.; Zeenat, L.; Bojedla, S.S.R.; Pati, F.; Zolfagharian, A.; Watts, D.C.; Bottino, M.C.; Bodaghi, M. Recent advances in additive manufacturing of patient-specific devices for dental and maxillofacial rehabilitation. *Dent. Mater.* **2024**, *40*, 700–715. [CrossRef] [PubMed]
68. Mamo, H.B.; Adamiak, M.; Kunwar, A. 3D printed biomedical devices and their applications: A review on state-of-the-art technologies, existing challenges, and future perspectives. *J. Mech. Behav. Biomed. Mater.* **2023**, *143*, 105930. [CrossRef] [PubMed]
69. Auriemma, G.; Tommasino, C.; Falcone, G.; Esposito, T.; Sardo, C.; Aquino, R.P. Additive Manufacturing Strategies for Personalized Drug Delivery Systems and Medical Devices: Fused Filament Fabrication and Semi Solid Extrusion. *Molecules* **2022**, *27*, 2784. [CrossRef] [PubMed]
70. Knetsch, M.L.W.; Koole, L.H. New Strategies in the Development of Antimicrobial Coatings: The Example of Increasing Usage of Silver and Silver Nanoparticles. *Polymers* **2011**, *3*, 340–366. [CrossRef]

Disclaimer/Publisher's Note: The statements, opinions and data contained in all publications are solely those of the individual author(s) and contributor(s) and not of MDPI and/or the editor(s). MDPI and/or the editor(s) disclaim responsibility for any injury to people or property resulting from any ideas, methods, instructions or products referred to in the content.